A Model Estimator for Noisy Compact Emission Recovery in Radio Synthesis Imaging

L. Zhang[1,2] , M. Zhang[3,4] , and B. Wang[1]

[1] College of Big Data and Information Engineering, Guizhou University, Guiyang 550025, People's Republic of China; lizhang.science@gmail.com
[2] State Key Laboratory of Public Big Data, Guizhou University, Guiyang 550025, People's Republic of China
[3] Xinjiang Astronomical Observatory, Chinese Academy of Sciences, Urumqi 830011, People's Republic of China
[4] Key Laboratory of Radio Astronomy, Chinese Academy of Sciences, Urumqi 830011, People's Republic of China

Abstract

Reconstruction of a noisy compact emission must consider not only the point-spread function but also the effect of noise. However, the traditional threshold method in widely-used CLEAN-based algorithms finds it difficult to effectively prevent noise in the model image during noisy compact-emission reconstruction. This significantly limits the performance in noisy compact-emission reconstruction, such as deep field imaging. There are two major difficulties in the accurate reconstruction of a Stokes-I image of compact emission: first, the threshold method that has been used in practice is difficult to use to separate compact emission and noise; and second, over-subtraction makes it difficult for the reconstructed Stokes-I model image to remain positive. Therefore, a filter-based denoizing mechanism is introduced in the search phase of the model components to separate signal and noise so that the signal can be effectively extracted. The relatively larger loop gain for positive components means that the reconstructed model is in line with astrophysics. This will reduce the errors between the true sky image and the model image. The new model estimator is tested on a simulated JVLA observation with realistic source distributions from the VLA Low-Frequency Sky Survey project and the SKADS/SCubed simulation. The experiments show that it is very effective when used to separate signal and noise to lower the noise in the model image. This work explores the use of existing common software CASA to achieve high dynamic range imaging, which is an important step toward square kilometer array data processing.

Unified Astronomy Thesaurus concepts: Astronomy data reduction (1861); Astronomy data analysis (1858)

1. Introduction

Radio interferometry synthesizes a virtual aperture of a diameter equivalent to the longest distance between the telescopes in an array. The measured data are often termed as visibilities or visibility function V^{ori}, which is the Fourier transformation of the true sky image I^{ori}(often termed the sky brightness function),

$$V^{ori} = FI^{ori}, \tag{1}$$

where F denotes the Fourier transform. This involves the van Cittert–Zernike theorem (Taylor et al. 1999; Thompson et al. 2017). In real measurements, only the noisy and incomplete samples V^{obs} of the true visibilities V^{ori} are available,

$$V^{obs} = SV^{ori} + SN^{obs}, \tag{2}$$

where S is the sampling function in the Fourier plane and N^{obs} is the noise in the measured visibilities. We obtain the dirty image I^{dirty} by computing the inverse Fourier transform of the measured visibilities V^{obs},

$$I^{dirty} = F^{-1}S(V^{ori} + N^{obs}). \tag{3}$$

We know from the convolution theorem of the Fourier transform theory that the dirty image is the convolution of the true sky image I^{ori} and the noise I^{noise} in the image plane (Bhatnagar & Cornwell 2004), and the dirty beam

$$B^{dirty} = F^{-1}S,$$

$$I^{dirty} = B^{dirty} * (I^{ori} + I^{noise}), \tag{4}$$

where $*$ is the convolution operator. I^{ori} is the sky signal. The noise I^{noise} comes from the sky, ground, and receiver in radio astronomy, which is one of the main factors that make image reconstruction difficult (Puetter et al. 2005). White noise and red noise are typically included in radio astronomical data. White noise is typically caused by thermal fluctuations, in which electromagnetic waves at all frequencies are proportionally present. It is considered to be highly random and can impact the sensitivity of radio antennas and systems. Meanwhile, red noise is often due to the nonlinearity of electronic devices, resulting in lower-frequency signals with higher intensity than their higher-frequency counterparts. Only white noise is discussed in this work.

Deconvolution in radio synthesis imaging is used to remove the sidelobes of the dirty beam in the dirty image, where both of them are known. One of the most successful deconvolution algorithms is the original Högbom CLEAN (Hg-Clean) algorithm (Högbom 1974; Thompson et al. 2017), which decomposes the true sky image as a collection of delta functions by finding the peaks of residual images and then removing the corresponding dirty beam from these peak points. To speed up the Hg-Clean algorithm, Clark (1980) improved it by using the fast Fourier transform (FFT) to compute the convolution between the model images and the dirty beam. The Cotton–Schwab algorithm (Schwab 1984) improved the Clark algorithm by executing the major-cycle subtraction of CLEAN components on the ungridded visibilities, which can effectively correct certain gridding errors. Recently, some scale-sensitive CLEAN

deconvolution algorithms (Bhatnagar & Cornwell 2004; Cornwell 2008; Rau & Cornwell 2011; Zhang et al. 2016, 2020, 2021b) have been proposed to represent extended emission more sparsely and effectively.

In the past 40–50 yr, this type of greedy (CLEAN-based) algorithm has been fully developed and has achieved significant results (Event Horizon Telescope Collaboration et al. 2019). In particular, the main focus in recent years has been on how to effectively reconstruct the extended features. However, a scene with noisy point sources is still a problem that remains unsolved. When noise and compact emission are comparable, it is difficult to distinguish between the two. This implies that without introducing separation techniques, a compact emission is hard to recover. A threshold approach, which is defined as a method that separates signal from noise by setting a threshold value, is usually employed in radio astronomy. While this approach has been widely-used in radio astronomical processing, it may not be suitable for some scenarios, such as in deep field imaging, where the noise level is comparable to the signal. More accurate reconstruction in scenarios such as source counting essentially requires the separation of noise and compact emission. Therefore, new approaches that can better handle the noise and point-spread function (PSF) sidelobe confusion should be explored.

In this paper, we introduce a new model estimator that is able to reconstruct point sources from a noisy observation. This study primarily addresses the challenges of imaging compact source scenes with noise in narrow-band observations, while disregarding issues related to broadband imaging.

In Section 2, the scale-free CLEAN for noisy compact-emission reconstruction and its problems will be described. In this section, we will discuss random noise represented by thermal noise (non-thermal sources of noise and the impact of these are not discussed in this paper) and confusion noise, which arises during the deconvolution process and becomes intertwined with random noise. Their combined effect plays a crucial role in the reconstruction of a noisy compact emission. In Section 3, we will describe the new model estimator, referred to as Denoizing-Clean (Dn-Clean) in this study, and provide its algorithmic details. In Section 4, some experiments will be described to demonstrate the performance of the new deconvolution algorithm. In Section 5, we simply conclude this algorithm.

2. Problems of Noisy Compact-emission Reconstruction

We know from Equation (4) that the image obtained by interferometry contains the effects of both the PSF and noise. This essentially requires a good model estimator to have the ability to eliminate both effects. However, the current common compact-emission estimators build models by continuously identifying the most reliable component with the maximum value from the residuals, and they then further eliminate the convolution effect of the PSF contained in a component. These methods are designed to remove the effect of the PSF sidelobes and can achieve good reconstruction effects in scenes with a high signal-to-noise ratio.

However, here we must mention "clean bias" (White et al. 1997; Rau et al. 2016). The deconvolution must be quite deep to effectively avoid a large amount of signal remaining in the residual, which is particularly crucial in scenarios such as high dynamic range imaging or deep field imaging. However, cleaning too deep will also cause a "clean bias" to

systematically suppress the signal, especially when the sidelobes are relatively large (Condon et al. 1998). For example, for VLA, the sidelobes of the dirty beam that are wider than the main lobe cause the area of one sidelobe to be larger than the area of the main lobe, which can cause the sidelobes of the diffuse emission to be brighter than the correct position, and false components will be reconstructed in these bright positions. However, the clean bias can be suppressed or eliminated to the greatest extent by adjusting the weight to obtain a dirty beam with fewer sidelobes (Condon et al. 1998) or improving the deconvolution algorithms (see the following contents or refer to Rau et al. 2016).

In addition, these existing deconvolution algorithms usually use noise threshold methods to separate and eliminate the effects of the noise. However, their performance will be significantly reduced in some scenes, such as deep field imaging, where the noise and PSF sidelobe confusion (Rau et al. 2016) are often not negligible. This happens because both the noise and compact emission can be perfectly represented as delta functions. When the amplitude of compact emission is less than or equal to the maximum value of the noise, then the noise and compact emission are no longer distinguishable in the peak search method. If the reconstructed signal level is above the maximum amplitude of the noise, then there may be a large amount of compact emission remaining in the residuals, which cannot be reconstructed. If the reconstruction goes deep (over-CLEANing), then a lot of noise will enter the model. Consequently, a large number of false sources will be introduced and it will be impossible to distinguish whether it is a real source or not. This could be unacceptable in data processing scenarios such as EoR imaging. Therefore, a noise cancellation mechanism for noisy compact emission must be included in the model estimator.

3. The Model Estimator

The proposed model estimator adopts the parametric model to solve the PSF problem. The mechanism of filter-based denoizing is introduced to realize the separation between noise and sky emission.

3.1. Filtering for Separation between Noise and Emission

Both noise and compact emission exist in the high-frequency part of Fourier space and are intertwined. However, the emission reconstruction simply pursues the high-frequency part, i.e., the image details. Filtered denoizing is a general technique in the field of signal and image processing. In this work, the noise in the residual image is suppressed by a filter operator T before the model component search,

$$I^{\text{filt}-\text{res}} = T * I^{\text{res}}, \tag{5}$$

where $I^{\text{filt}-\text{res}}$ is the filtered residual image and there are many options for the filter T. In general image processing, a low-pass filter is usually used to achieve noise cancellation (Gonzalez & Woods 2010). This is particularly important for source identification/detection (Portillo Stephen et al. 2017; Vafaei Sadr et al. 2019) in the deconvolution process. Such methods have been widely-used in the multi-scale reconstruction of diffuse emissions in astronomy (Bhatnagar & Cornwell 2004; Cornwell 2008; Rau & Cornwell 2011; Zhang et al. 2016). However, there is no good strategy to deal with noise in the

conventional scale-free CLEAN algorithms that are used for compact-emission reconstruction.

3.2. Parameterization for Compact Emission

When the noise is separated from emission, the representation of the compact emission is another important issue in reconstructing it. The delta functions or points are undoubtedly a very good representation of compact emission (Rau 2010). In this work, we follow the basic idea that delta functions represent compact emission. A credible model image I^{model} with a limited number of delta functions (points) is used to approximate sky emission,

$$I^{\mathrm{ori}} = I^{\mathrm{model}} + \epsilon_o = \sum_{k=1}^{L} I_k^{\mathrm{amp}} \delta_k(x - x_k, y - y_k) + \epsilon_o, \quad (6)$$

where ϵ_o is the error between the model image I^{model} and the true sky image I^{ori}.

However, some new parameterization strategies have been introduced for better model estimation. Scale-free algorithms only introduce the scale prior, but not the amplitude prior. In fact, the amplitudes are only adjusted by a fixed loop gain, which will cause the over-subtraction of some amplitudes. For compact-emission reconstruction, these negative components mainly come from correcting the over-subtraction caused by a fixed loop gain. Different loop gains for positive and negative components to solve the problem of negative component reconstruction caused by over-subtraction have been successfully applied in diffuse emission reconstruction (Zhang et al. 2021a). This strategy has been proven to effectively reduce the negative components during deconvolution in the Stokes-I model image, ensuring the positiveness of the model, which makes it easier to impose strict non-negative restrictions during the major cycle of the CLEAN deconvolution. In this study, non-unique loop gins are integrated into our proposed model estimator for compact-emission reconstruction. A conservative method to balance between the positive characteristics of the model image and the necessity of negative components during deconvolution uses a smaller loop gain for negative components. This works well when the loop gain g for negative component is half of the loop gain for positive components.

$$g = \begin{cases} a, & I_k^{\mathrm{amp}} > 0, \\ 0.5a, & I_k^{\mathrm{amp}} <= 0, \end{cases} \quad (7)$$

where a is the value of loop gain for positive components. At the same time, just like the existing CLEAN-based algorithms, standard deviation is used as a stopping criterion, which helps to judge whether the residuals have reached the noise level. These methods can help us to find a better model image to approximate the true sky image.

3.3. The New Reconstruction Algorithm

These ideas form a new model estimator in the following ways. Before searching each model component, the noise and sky emission have been separated, allowing the sky emission to be visible from the noisy image. Our parameterization process is then used to construct each component. The specific process to solve this reconstruction problem is as follows.

1. Filter the current residual image I_k^{res} (the dirty image for the first time) with a low-pass filter T.

2. Find the delta component which is the absolute peak located in the point (x_k, y_k) in the smoothed residual image, and the corresponding amplitude is I_k^{amp} in I_k^{res}. It is worth mentioning here that the sources of interest are first separated from the noisy image and they are then removed from the full-resolution dirty/residual image.

3. Update the residual image $I_k^{\mathrm{res}} = I_{k-1}^{\mathrm{res}} - gB^{\mathrm{dirty}} * I_k^{\mathrm{amp}}(x_k, y_k)$. The smoothed residual image obtained in the first step was also updated in this step. The loop gains g are different for positive and negative components.

4. Update the model image I_k^{model}.
   Repeat steps 2–4 unless the standard deviation of the current residual image is less than 50% of the residual image in the last major cycle (see the next step).

5. Compute the residual image of the major cycle $I^{res-major}$ by predicting the current model image onto ungridded visibilities, and then computing the inverse Fourier transform of the difference between the predicted visibilities and the measured visibilities, $I^{res-major} = A^{\dagger}(V^{\mathrm{obs}} - AI^{\mathrm{model}})$, where A denotes all operations from the model image to the predicted ungridded visibilities and $A^{\dagger}$ is the inverse operations of A.
   Repeat steps 1–5 unless the standard deviation of the last residual image is less than the noise level.

6. Make the CLEAN image I^{clean}.

7. Compute the restored image I^{restored} by adding the residual image into the CLEAN image.

Steps 2–4 are termed as the minor cycle and the steps 1–5 are termed as the major cycle (Rau 2010; Rau & Cornwell 2011). In the sense of optimization, the estimation of the model image in the minor cycle is equivalent to minimizing the objective function χ^2 (Zhang et al. 2020),

$$\chi^2 = \| I^{\mathrm{dirty}} - B^{\mathrm{dirty}} * I^{\mathrm{model}} \|_2^2, \quad (8)$$

where $\| \ \|_2^2$ is the L_2 norm. According to Equation (4), the above equation can be written as,

$$\chi^2 = \| B^{\mathrm{dirty}} * (I^{\mathrm{ori}} + I^{\mathrm{noise}}) - B^{\mathrm{dirty}} * I^{\mathrm{model}} \|_2^2. \quad (9)$$

This work focuses on the case of noisy compact emission. The purpose is to separate the noise and compact emission before the component search, so that the correct component can be found easily and more accurately from the dirty image after noise suppression. Noise suppression can be obtained by convolving a low-pass filter,

$$I^{\mathrm{filt-dirty}} = I^{\mathrm{dirty}} * T = B^{\mathrm{dirty}} * (I^{\mathrm{ori}} + I^{\mathrm{noise}}) * T, \quad (10)$$

where $I^{\mathrm{filt-dirty}}$ is the denoized dirty image. According to the nature of the convolution (Gonzalez & Woods 2010), the filter T is equivalent to directly acting on the noisy image determined by the formula $I^{\mathrm{ori}} + I^{\mathrm{noise}}$, and then convolving with the PSF B^{dirty}. The filtered dirty image is represented as follows,

$$I^{\mathrm{filt-dirty}} = B^{\mathrm{dirty}} * (I^{\mathrm{ori}} + I^{\mathrm{noise}}) * T = B^{\mathrm{dirty}} * (I^{\mathrm{ori}} - \epsilon_d), \quad (11)$$

where ϵ_d is the difference between the filtered noisy image $(I^{\mathrm{ori}} + I^{\mathrm{noise}}) * T$ and the true sky image I^{ori}. ϵ_d comes from two parts. One part is the difference between I^{ori} and $I^{\mathrm{ori}} * T$, and the other part is the residuals after filtering of the noise I^{noise}. And
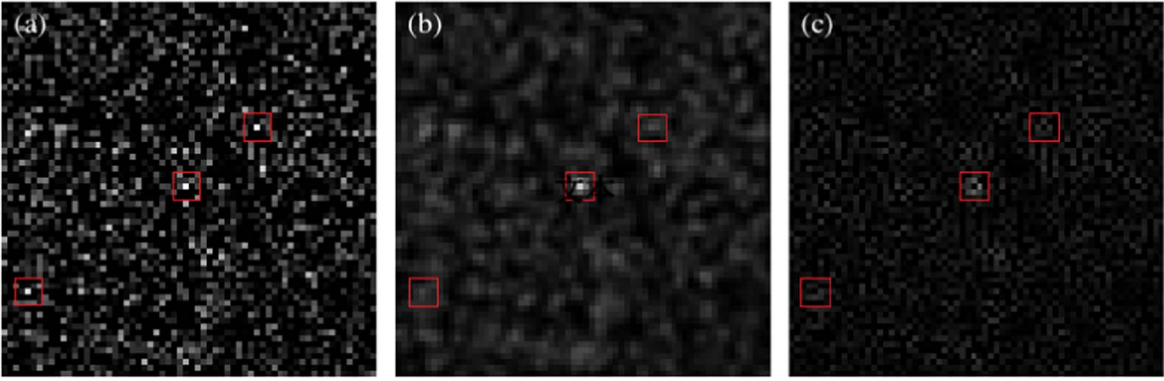
Figure 1. Simulation of denoizing. (a) the noisy image degraded by a Gaussian noise distribution with PSNR of 22.92 dB, peak of 0.038 mJy and noise level of 0.0024 mJy; (b) the denoized image with PSNR of 26.59 dB, peak of 0.012 mJy, and noise level of 0.0009 mJy; (c) the differences/errors between the noisy and denoized images. The middle point marked by the red box is the simulated compact source and the other two red boxes are noise points.
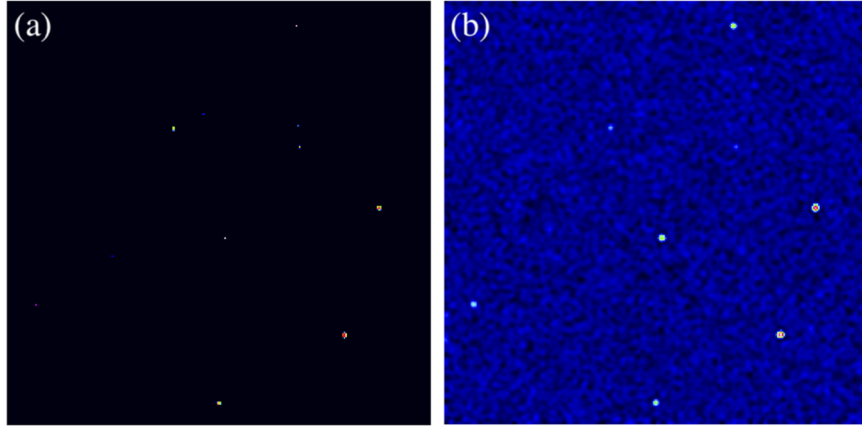
Figure 2. Results from the simulation of JVLA observation with a VLSS distribution: (a) the reference distribution/image; (c) the observed/dirty image with the effects of the PSF and noise.

so,

$$\epsilon_d = (I^{\mathrm{ori}} - I^{\mathrm{ori}} * T) - I^{\mathrm{noise}} * T. \qquad (12)$$

This filtering technique is capable of effectively suppressing noise while preserving compact emission. A low signal-to-noise ratio filtering experiment was done to demonstrate its effectiveness. The middle point marked by the red box in Figure 1 is the simulated compact source and the other two red boxes are noise points. By comparing Figures 1(a) and (b), it can be seen that filtering can significantly suppress noise and that compact emission has been revealed. This effectively separates the noise and compact sources, and preserves compact emission so that the noise cannot enter the model image. Figure 1(c) shows the difference before and after filtering. This error in Figure 1(c) is allowed and will be corrected in the major cycle (please refer to the algorithm flow above). The core purpose here is to expose compact emission from noisy observations so that it can be accurately found. Existing scale-sensitive CLEAN algorithms (Bhatnagar & Cornwell 2004; Cornwell 2008; Rau 2010; Zhang et al. 2016) have a similar approach, but for extended emission (i.e., multi-scale features). In the adaptive scale CLEAN algorithms (Bhatnagar & Cornwell 2004; Zhang et al. 2016), the correlation length is used for the basic separation of extended features and noise. The term involving noise N^{obs} in the Equation (2) can be regarded as a Gaussian random process (Thompson et al. 2017), whose pixel-to-pixel noise is independent (i.e., zero correlation length; Bhatnagar & Cornwell 2004). Since

the correlation length of the extended feature is bigger than zero, for the noisy image $I^{\mathrm{ori}} + I^{\mathrm{noise}}$, the extended feature and noise can be distinguished by the correlation length. In a dirty image containing a PSF, noise is also affected by the PSF. At this time, the extended feature has the minimum correlation length of the resolution element (the synthesized beam), and the upper limit of the correlation length of noise and compact emission is the resolution element (Bhatnagar & Cornwell 2004). This can distinguish extended features and noise in dirty images. However, the traditional threshold method is still used to separate compact emission and noise, and it is widely-known that they cannot be separated well. The fundamental reason why compact emission and noise cannot be separated well is that they have the same correlation length in the noisy image $I^{\mathrm{ori}} + I^{\mathrm{noise}}$ and the dirty image. In the reconstruction process, there is also confusion noise (which is applicable to the above analysis).

In the case of noisy compact emission, we use filtering methods to preliminarily separate compact emission and noise. This is a common method in the field of signal processing (Gonzalez & Woods 2010). Combined with the Equations (10)–(8)–(4), the objective function in the proposed algorithm is written as,

$$\chi^2 = \| B^{\mathrm{dirty}} * (I^{\mathrm{ori}} + I^{\mathrm{noise}}) * T - B^{\mathrm{dirty}} * I^{\mathrm{model}} \|_2^2$$
$$= \| B^{\mathrm{dirty}} * (I^{\mathrm{ori}} - \epsilon_d) - B^{\mathrm{dirty}} * I^{\mathrm{model}} \|_2^2. \qquad (13)$$

What needs to be solved now is to find the most suitable model image I^{model} by minimizing this objective function (13).
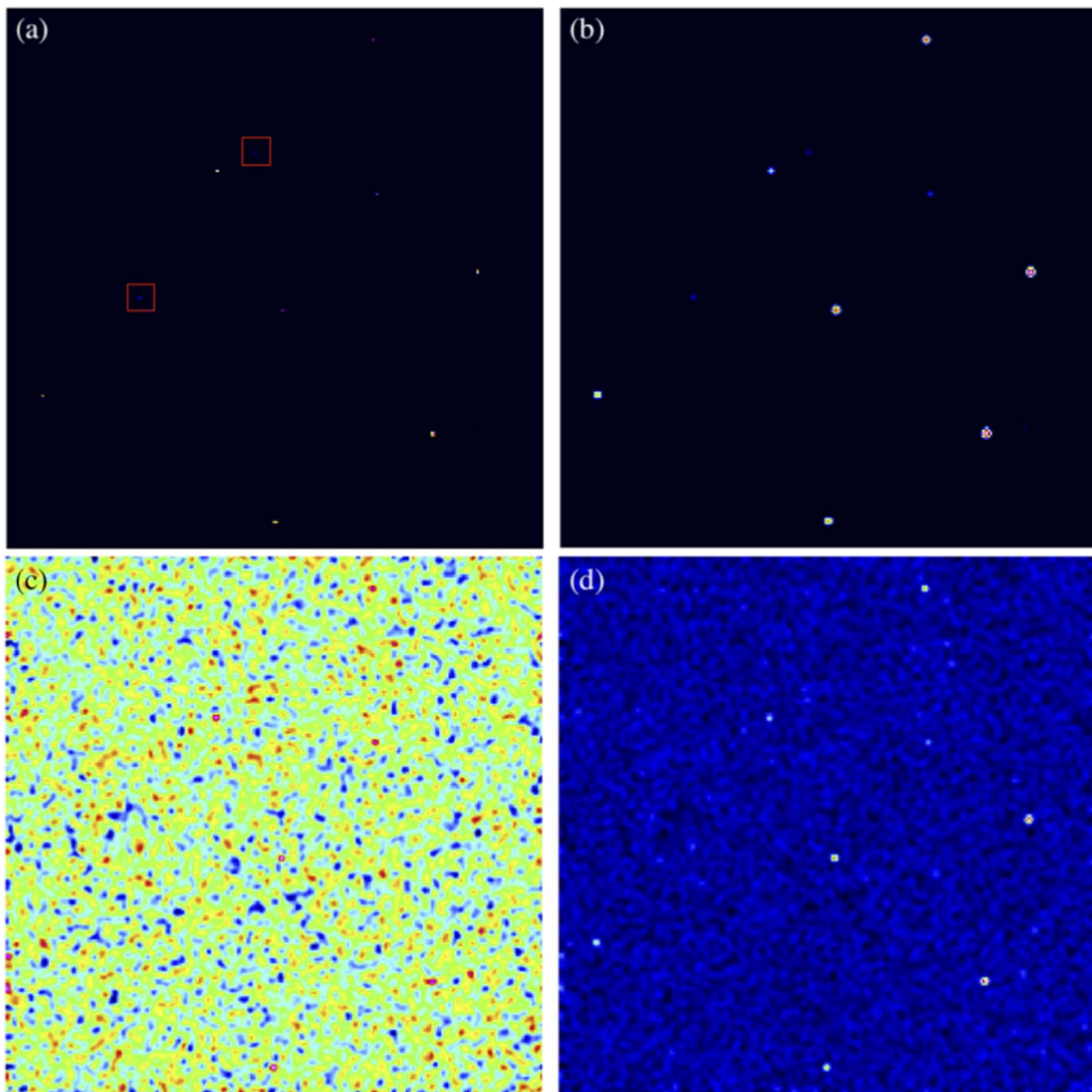
Figure 3. Reconstruction results from the proposed model estimator: (a) the reconstructed model image; (b) the smoothed model image convolved with the CLEAN beam; (c) the residual image; (d) the restored image (the smoothed image + the residual image).
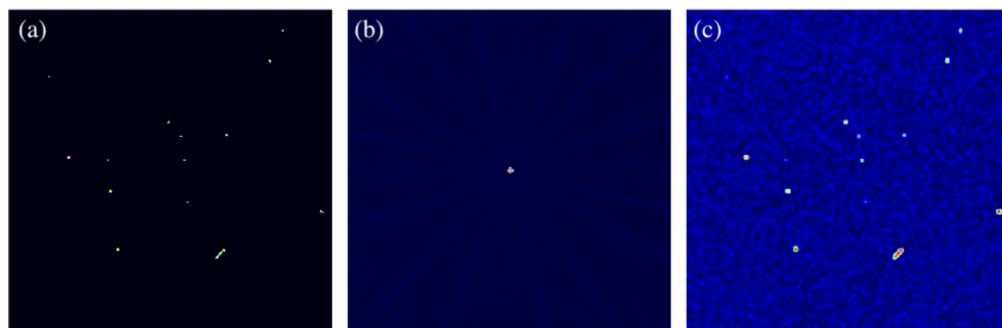

Figure 4. Another JVLA observation simulation of a VLSS distribution with more compact sources and a strip-shaped extended structure. (a) the reference distribution; (b) the PSF with non-negligible sidelobes; (c) the dirty image with the effects of the PSF and noise.

The errors caused by the separation of compact emission and noise, as well as other errors such as gridding (Rau 2010), can be corrected in the major cycles.

To find the minimum value of the objective function, the first derivative provides the update direction in the proposed algorithm (Bhatnagar & Cornwell 2004; Zhang et al. 2020),

$$\frac{\partial \chi^2}{\partial p_k} \equiv \frac{\partial \chi^2}{\partial I_k^{\mathrm{amp}}} = -2[I_k^{\mathrm{res}}]^T \frac{\partial p_k}{\partial I_k^{\mathrm{amp}}} = -2\max(I_k^{\mathrm{res}}), \quad (14)$$
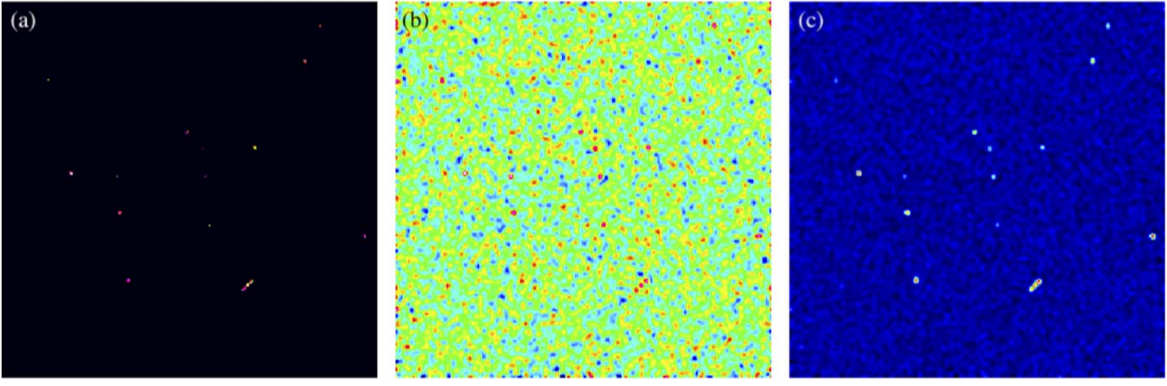
Figure 5. Reconstruction results from the proposed model estimator: (a) the reconstructed model image; (b) the residual image; (c) the restored image.

where

$$I_k^{\text{res}} = I_{k-1}^{\text{res}} - gB^{\text{dirty}} * I_k^{\text{amp}}, \qquad (15)$$

where $p_k = I_k^{\text{amp}}$ and $max()$ find the absolute peak of the current residual image I_k^{res}. The peak search from the current residual image is equivalent to minimizing the objective function along the axis of the largest derivative. Finding the peak point is a fast implementation of the computation of the first derivative. In the major cycle, deconvolving to the noise level is equivalent to minimizing the following equation (Cornwell & Wieringa 1997; Bhatnagar & Cornwell 2004; Rau & Cornwell 2006; Bhatnagar et al. 2008; Rau et al. 2009; Rau & Cornwell 2011),

$$\chi^2 = \|V^{\text{obs}} - AI^{\text{model}}\|_2^2. \qquad (16)$$

The optimal model will fit the measured visibilities best.

3.4. Implementation

To separate signals and noise, the noise needs to be filtered by a low-pass filter during the search phase of model components. This filter can take many forms (Gonzalez & Woods 2010), but in this implementation we choose a Gaussian low-pass filter. Mathematically, a filter function is implemented by a convolution between the residual image and a Gaussian function,

$$I^{\text{filt-res}} = G * I^{\text{res}}, \qquad (17)$$

where $I^{\text{filt-res}}$ is the residual image after smoothing and G is computed by the following function,

$$G(x, y) = \frac{1}{2\pi\sigma^2} e^{-\frac{x^2+y^2}{2\sigma^2}}, \qquad (18)$$

where x and y are the distances from the origin in the horizontal and vertical axes, respectively, and σ is the standard deviation. The Fourier transform of a Gaussian function is another Gaussian function. So smoothing the residual image is equivalent to suppressing the noise in the residual image. In other words, the noise is suppressed in the component search phase. Thereby, it is difficult for noise to enter the model image used to approximate the true sky image under the same conditions. This achieves the separation between the signals and noise.

The propagation of the error ϵ_d can be suppressed by simply updating the residuals from the dirty image,

$$I_k^{\text{res}} = I^{\text{dirty}} - B^{\text{dirty}} * I_k^{\text{model}}. \qquad (19)$$

After each update, it is necessary to re-separate compact emission and noise using Equation (17) in the new residual image I_k^{res}. However, the convolution that is used to separate compact emission and noise is performed only a few times or even once for each major cycle, resulting in a good performance (see Section 4), so it is computationally cheap.

Although this method is similar to the tapering technique (Rau 2010; Thompson et al. 2017), there are some differences. In tapering, the effects of smoothing on the dirty image are fixed and the error caused by smoothing cannot be corrected in the deconvolution process. Our method can correct this error during deconvolution. Simultaneously, we have found that it works well when the standard deviation of the Gaussian filter function is several times that of the noise.

This new algorithm is similar to the Cotton–Schwab CLEAN algorithm, both predict the intermediate model to ungridded points and compare it with the original measured visibilities to reduce errors. The main difference is that our model estimator uses a new method to prevent noise from entering the model and uses different loop gains to optimize the model. It is these differences that give the new algorithm a better performance for noisy compact-emission reconstruction. Python and the Common Astronomy Software Applications package (CASA) are used to jointly implement this work. The Högbom algorithm[5] and the minor cycle of the proposed algorithm are implemented in Python. The major cycle of the proposed algorithm is implemented by calling some functions of the CASA.

4. Numerical Experiments and Comparisons

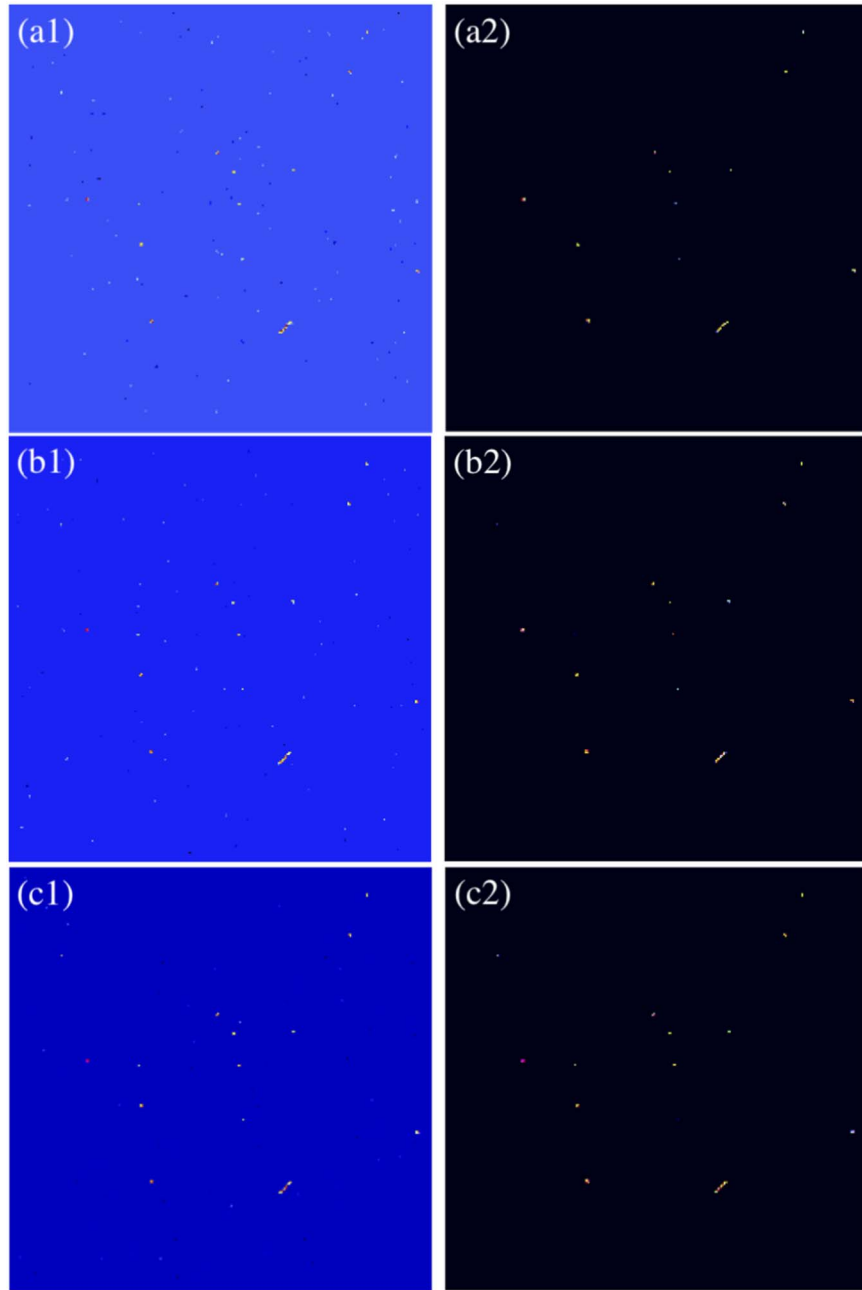### 4.1. Reconstruction for Faint and Compact Emission

To illustrate the motivation of the proposed model estimator, we apply it to the simulated JVLA[6] observation data. The distribution in Figure 2(a) is from the VLA Low-Frequency Sky Survey (VLSS) project.[7] It is obtained by removing the noise and extended sources larger than 9 pixels from the

---

Figure 6. Model images from the Hg-Clean and our model estimator. The first column comes from the Hg-Clean and the second column comes from our model estimator. The first to third lines are reconstructed from the dirty images of about 30, 31, and 33 dB for PSNR, corresponding to the peak values of 30σ, 35σ, and 45σ in the reference distribution respectively. The weakest signal in the reference distribution is comparable to the level of noise. $N\sigma$ here refers to the ratio of the peak value in the reference distribution to the noise level. The noise level is measured by the rms, i.e., σ. These results are reconstructed with the CLEAN threshold of 3σ. The details are as follows: (a1) from the Hg-Clean with 30σ; (a2) from our model estimator with 30σ; (b1) from the Hg-Clean with 35σ; (b2) from our model estimator with 35σ; (c1) from the Hg-Clean with 45σ; and (c2) from our model estimator with 45σ.

original data. The CASA is then used to do a simulated observation for the reference distribution. The simulated observations were performed in the Ls-band with a bandwidth of 1 GHz and 32 channels, and lasted for a duration of 6 hr. Gaussian white noise was added to the measured visibilities for the purposes of our project research. The observed image (i.e., dirty image) is shown in Figure 2(b). It can be seen that the sources have been degraded by the PSF and the dirty image is full of noise; some sources have been submerged by the noise and the PSF. Our task is to eliminate the effects of the PSF and noise, i.e., to recover the sources in the reference distribution from the dirty image.

The reconstructed results using our model estimator are shown in Figure 3. The reconstructed model image (Figure 3(a)) has recovered all of the sources, except for one faint and compact source that is not originally visible in the dirty image. The two faint and compact sources in the red boxes have been completely submerged in the noise of the dirty image. However, our model estimator can reconstruct them well. The smoothed model image convolved by the CLEAN beam is shown in Figure 3(b), and it no longer has the effect of the PSF sidelobes. In this image, the two faint and compact sources are clearly visible. If we look at the restored image (Figure 3(d)), then these two sources are not visible. This

Table 1
Statistics of the Number of Reconstructed Sources from Different Noise Levels

PSNR (dB)	Hg-Clean Recon / False	Dn-Clean Recon / False
30	14/138	13/0
31	14/115	14/0
33	14/104	14/0

Note. "PSNR" denotes the Peak Signal-to-Noise Ratio, "Recon" represents the number of sources reconstructed from the reference distribution, and "False" refers to the noise entering the model. In this example, there are 14 sources in the reference distribution. All results come from 3σ reconstruction.

Table 2
Quantity Statistics of Reconstruction Sources from Different Reconstruction Levels

Reconstruction Levels	Hg-Clean Recon / False	Dn-Clean Recon / False
2.5σ	14/104	14/0
3.5σ	14/44	14/0
4.5σ	4/0	4/0

Note. These reconstruction results come from 2.5σ, 3.5σ and 4.5σ reconstructions respectively.

Table 3
Source Number and Mean Value of Error Distributions of SKADS/SCubed Simulation Data with Low Dynamic Range

Algorithms	$s > 35.1$ uJy Number	$s > 35.1$ uJy Mean	$s > 152.1$ uJy Number	$s > 152.1$ uJy Mean	$s > 250.0$ uJy Number	$s > 250.0$ uJy Mean
Hg-Clean	**1458**	**0.954**	455	0.996	294	1.002
Dn-Clean	**2930**	**0.997**	446	0.997	291	1.004

Note. "Number" of reconstructed sources is counted at all true source pixels of the reference image. "Mean" is the Mean Value of Error Distributions.

shows that these two faint and compact sources are below the noise level. This illustrates the effectiveness of the proposed model estimator well.

To further verify the performance of our model estimator, another simulated observation with a realistic VLSS distribution was performed. The simulated observation process is similar to the first experiment. The reference distribution (Figure 4(a)) has more compact sources and a strip-shaped extended structure. The simulated results of the observation with the noise and PSF effects are shown in Figure 4(b). The reconstructed results are shown in Figure 5. Compared to the reference distribution, the model from the proposed model estimator (Figure 5(a)) reconstructs all the sources, including some sources below the noise level (which can be seen by comparing the restored image with the reference distribution).

The reconstructed image of our model estimator is compared with that of the conventional method (the Hg-Clean algorithm), as seen in Figure 6. It can be seen that our model estimator can reconstruct the sources well at different noise levels. However, this is not the case with the conventional Hg-Clean algorithm. As the signal-to-noise ratio of the noise decreases, more noise will enter the model image. The statistical results of the number of sources in the model images are shown in Table 1. This also shows that the false sources from the noise in the reconstructed image will continue to increase as the signal-to-noise ratio decreases. Our experiments also indicate that aside from the number of point sources of the reference image, there is an approximately equal number of positive and negative sources in the reconstructed images. This suggests that the erroneously reconstructed point sources are highly likely a result of noise, which is a problem that cannot be effectively addressed through conventional thresholding methods.

To further demonstrate the effectiveness of the proposed algorithm, different reconstruction levels of 2.5σ, 3.5σ, and 4.5σ were done, and the results are shown in the Table 2. It can be seen that the conventional method results in a lot of noise entering the model when the reconstruction is near or below 3σ, and more noise will enter the model as the reconstruction deepens. However, the proposed model estimator is not significantly affected by the noise and is able to reconstruct the sources well from a noisy compact emission. At the same time, if the reconstruction level is much higher than 3σ, then neither method can reconstruct faint sources. The experiments in this study show that the proposed model estimator can do a deeper reconstruction than the Hg-Clean algorithm, which enables it to perform high dynamic range reconstruction. Furthermore, since filtering involves a convolution operation, which is computationally cheap, the CLEAN time will not be significantly increased.

4.2. Error Distributions and CLEAN Bias

A new reference distribution with more crowded point sources from the SKADS/SCubed simulated sky project (Wilman et al. 2008) is simulated as an JVLA observation (see Figure 7) to further verify the performance of the proposed model estimator. This experiment is similar to the previous simulated observations, but with a higher sidelobe level of 0.025. The reference distribution has a data range of 7 uJy– 8 mJy. The noise level in the dirty image is 12.7 uJy. The restored image is shown in Figure 8. Upon close inspection, it may be noted that when sources are particularly close to the edge of the image, the restored image of the Hg-Clean algorithm (Figure 8(a)) has more obvious sidelobe structures, while that of our model estimator (Figure 8(b)) shows slight false features, albeit less visibly. This may be attributed to the fact that our proposed estimator has better denoizing capabilities.

Figure 9 shows the error distributions (imaging fidelity) of the two algorithms, which is the ratio of the reconstructed model to the reference image located at all true source pixels (Rau et al. 2016). We counted the number of sources reconstructed above 35.1 uJy, 152.1 uJy, 250 uJy, and error distributions (see Figure 9). Figure 9 and Table 3 show that there is no significant difference between the two algorithms in restoring strong sources (sources that are significantly higher than noise levels), but the proposed model estimator can reconstruct fainter sources.

The CLEAN bias is a well-known system shift, in which reconstructed intensities tend to be lower than expected values. This is common for deep imaging with large amounts of closely spaced faint sources (Rau et al. 2016). When the reconstruction is below 3σ (35.1 uJy = 2.76σ), the mean value of error distributions of the Hg-Clean algorithm is 0.954 (see Table 3), i.e., there is a systematic downward shift—CLEAN bias, while our model estimator has a mean value of 0.997 close to 1.0, which shows that our model estimator does not
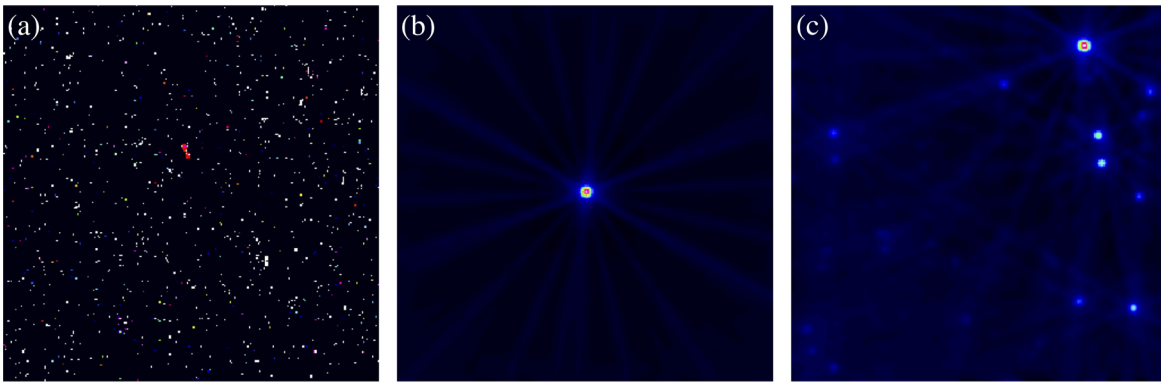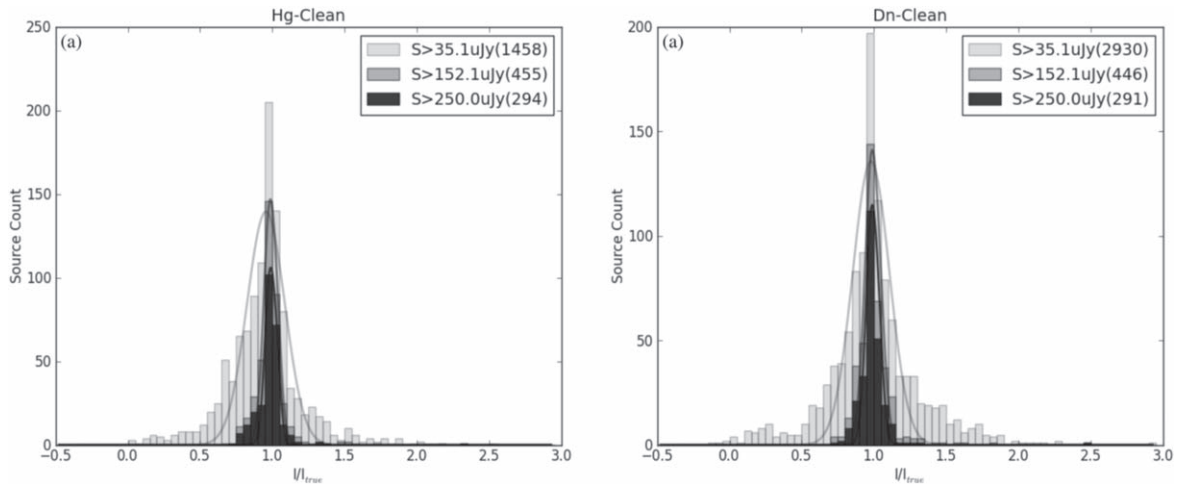
Figure 7. Simulation of the SKADS/SCubed data: (a) the reference image which is displayed only from 7 uJy to 10 uJy for more faint sources; (b) the dirty image with a natural weighting displayed at the full date range.
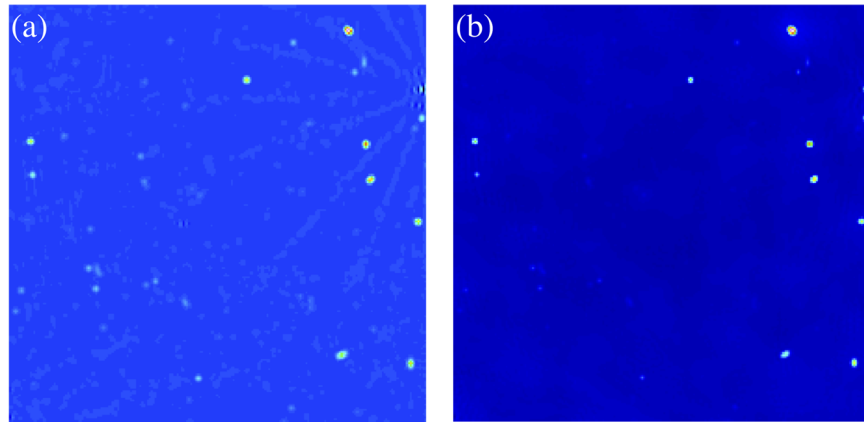
Figure 8. Restored images of the SKADS/SCubed data.:(a) from the Hg-Clean algorithm; (b) from the proposed model estimator. These two images are displayed by the logarithmic scaling with CASA parameter "scaling power cycles" of -1.3.
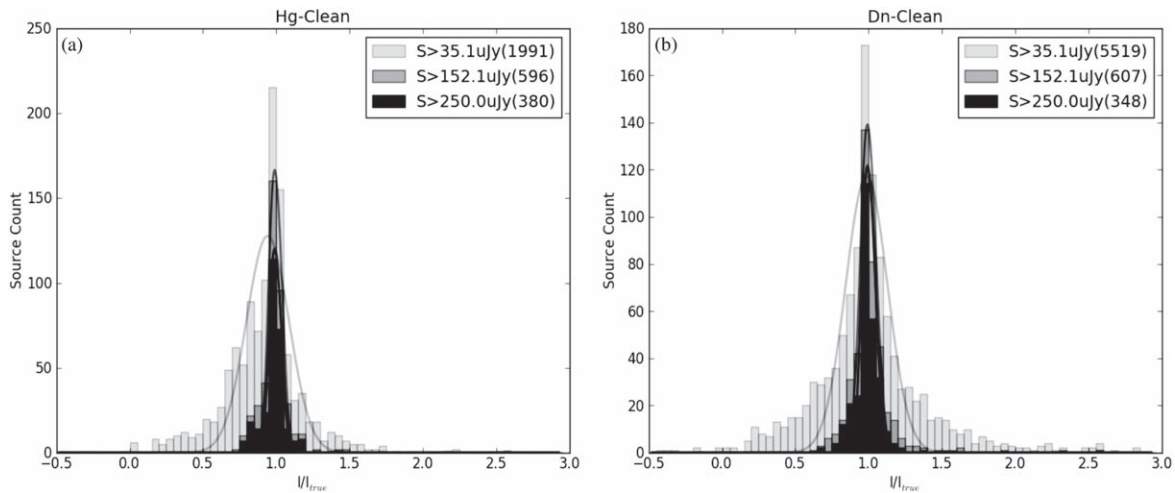

Figure 9. Error distributions as a function of source brightness with low dynamic range of the SKADS/SCubed data: (a) from the Hg-Clean algorithm; (b) from the proposed model estimator. The histogram plots the points of the restored image above 35.1 uJy, 152.1 uJy, and 250 uJy at all the locations of the true source pixels, respectively. The corresponding Gaussian functions are fitted to these histograms without the position of 1.0.

have such a bias. This test is repeated in a high dynamic range case with an addition of 100 mJy in that reference image. We can get the same conclusion from the high dynamic range experiment (see Figure 10 and Table 4).

It can be seen that the performance of the proposed model estimator in reconstructing noisy compact emission is significantly higher than that of the conventional CLEAN-based method (in terms of faint source reconstruction and CLEAN bias in these experiments). This happens because the proposed model estimator contains strategies for dealing with both noise and PSF, while the conventional CLEAN-based method only has the PSF elimination strategies. The

Figure 10. Error distributions as a function of source brightness with high dynamic range of the SKADS/SCubed data: (a) from the Hg-Clean algorithm; (b) from the proposed model estimator. The histogram plots the points of the restored image above 35.1 uJy, 152.1 uJy, and 250 uJy at all the locations of the true source pixels, respectively. The corresponding Gaussian functions are fitted to these histograms without the position of 1.0.

Table 4
Source Number and Mean Value of Error Distributions of SKADS/SCubed Simulation Data with High Dynamic Range

	$s > 35.1$ uJy		$s > 152.1$ uJy		$s > 250.0$ uJy	
Algorithms	Number	Mean	Number	Mean	Number	Mean
Hg-Clean	**1991**	**0.930**	596	0.995	380	1.006
Dn-Clean	**5519**	**1.007**	607	1.004	348	1.009

Note. "Number" of reconstructed sources is counted at all true source pixels of the reference image. "Mean" is the Mean Value of Error Distributions.

proposed model estimator with non-unique loop gains and a separation mechanism of signal and noise that can reconstruct the signal more accurately to effectively reduce CLEAN bias.

4.3. Discussion

The elimination of PSF is a problem that must be solved in the field of astronomical imaging (Jia et al. 2017; Thompson et al. 2017; Sun et al. 2021). The key idea of this work is to do the separation between noise and compact sources to realize the goal of restoring faint compact sources. In these experiments, we demonstrated the work from different perspectives using different data.

Random noise vs confusion noise: When using a telescope array to measure astronomical data, various types of noise can enter the data and become intertwined with it. The presence of noise can greatly impact the accuracy of the reconstruction process, particularly when dealing with data that exhibits low signal-to-noise ratio. Recovering an emission from compact sources in the presence of noise is especially challenging because both noise and compact sources can be accurately represented by delta functions.

Furthermore, the confusion noise introduced by the PSF and the reconstruction process itself present a significant challenge to the reconstruction of astronomical data. Fortunately, compact emission and confusion noise can both be represented using the same function. The key to achieving deep reconstructions and enabling high dynamic range imaging, such as in the case of Epoch of Reionization (EoR) imaging

(Bonaldi 2018), lies in separating the different sources of noise and emission.

In summary, the separation of different types of noise and sources is a crucial step in the accurate reconstruction of astronomical data, particularly in the presence of noise and confusion noise. By employing appropriate methods to separate these sources, we can achieve high-quality reconstructions and uncover new insights into the workings of the universe.

Reconstruction of faint compact emission: The reconstruction problem of faint compact emission has always been a considerable challenge. As mentioned above, both noise and compact emission can be represented perfectly by delta functions. Therefore, to reconstruct faint compact emission, the sources must be separated from the noise. Random noise and true emission have significantly different statistical characteristics, which allow us to separate them using an appropriate separation mechanism. As in Figure 1, the denoizing method effectively separates noise from sources. This allows the sources to be reconstructed more accurately. From the first experiment (see Figure 3), it can be seen that the proposed model estimator can effectively restore compact sources under the noise, but the traditional method finds it difficult to do that. At the same time, these experiments used the reference distributions from noisy low-density compact emission to noisy crowded compact emission, and the experiments showed that the proposed model estimator was able to perform well at different densities.

Signal-to-noise separation versus sources of outlier fields: In the experiment, the amount of noise added is displayed in the second column of Table 5. Considering the previous experiments in this paper, it can be concluded that the Dn-Clean method is more accurate in recovering the number of sources and has less CLEAN bias, and its residual rms is closer to the added noise. This clearly demonstrates that our method has better signal-to-noise separation capability.

However, it is also worth noting that the residual rms of Dn-Clean is still not exactly the same as the added noise rms in Table 5. This may be due to two main reasons. First, the sidelobe effect of outlier fields.[8] In our experiment, we chose

---

[8] https://casaguides.nrao.edu/index.php?title=VLA_CASA_Imaging-CASA6.5.2#Imaging_Outlier_Fields

Table 5
The rms of Dirty and Residual Images of SKADS/Scubed Simulation Data

	Noise rms in dirty image	Residual rms of Hg-Clean	Residual rms of Dn-Clean
Experiments of Figure 9	1.254×10^{-05}	5.318×10^{-06}	5.584×10^{-05}
Experiments of Figure 10	1.265×10^{-05}	6.597×10^{-06}	9.542×10^{-05}

dense point sources from SKADS/Scubed simulation data and used masking techniques to prevent edge effects, which resulted in no deconvolution of the 15 pixels near the edge. The psf sidelobe effect of sources in this region may affect the middle sources, which could be a reason why the residual rms of Dn-Clean is higher than the original (added) noise rms. Second, there are a small number of extended sources within the field of view of SKADS/Scubed simulated survey data, and the Dn-Clean algorithm based on scale-free decomposition is unable to accurately model the extended features (Zhang et al. 2020). Overall, the Dn-Clean method has better signal-to-noise separation capabilities.

Stopping threshold and Over-CLEANing: The noise and compact emission have the same correlation length (the order of the resolution element), so that they cannot be separated using the correlation length. The traditional approach is to use an amplitude threshold to separate compact emission from the noise. Such a traditional stopping threshold method can only accurately separate compact emission that is significantly higher than the noise level. Compact emission below the noise level cannot be recovered. If deconvolution goes too deep (over-CLEANing), then a large amount of noise that is indistinguishable from true compact emission enters the model image, so that the reconstructed model image is far from the potential true sky image. From the second experiment, Figure 6 and Table 2 show that our method has better reconstruction performance at different noise threshold levels.

Different noise levels: Different noise levels often significantly affect the quality of the reconstructed images. In the second experiment, we tested the performance of the proposed model estimators and the traditional Hg-Clean method with the distribution of the same compact emission at different noise levels. Figure 6 and Table 1 show that as the signal-to-noise ratio decreases, a large amount of noise has entered the images reconstructed by the traditional deconvolution method, but the proposed model estimator has not been significantly affected.

CLEAN bias: Clean bias, which is common in the case of crowded compact sources, is a phenomenon where the reconstructed emission tends to be lower than expected values. In the test with this SKADS/SCubed simulation data, in Figures 9–10 and Tables 3–4 it can be seen that the traditional Hg-Clean algorithm has shown significant CLEAN bias in the cases of different dynamic ranges but the proposed estimator does not.

Reconstruction for Stokes-I images: In our method, a more accurate model of a Stokes-I image is reconstructed by a denoising algorithm used to separate sources from noise and non-unique loop gains used to prevent negative components from entering the reconstructed model. In Stokes-I image reconstruction, the negative components are necessary for the reconstruction process (Zhang et al. 2020) but its model image physically requires a positive component. Therefore, a smaller loop gain is used to suppress negative components from entering the model.

5. Summary

CLEAN-based algorithms are already a general method of compact-emission reconstruction. This method uses the delta functions to represent compact emission, which is theoretically perfect when the noise is negligible. Therefore, this method can well-reconstruct compact emission in the case of high signal-to-noise ratio. However, when the noise is not negligible or the compact emission below the noise level needs to be restored, this method experiences great difficulty. The root cause is that there is no good strategy for separating signals from noise in this method. In this work, we propose a new model estimator, which can effectively separate noise and the sources, and estimate compact emission from a noisy dirty image. This model estimator still uses the delta functions as the basic model for compact-emission parameterization. At the same time, the filtering-based strategy is introduced to separate signals and noise, so that faint sources are visible during the reconstruction process. Building upon this work, there are opportunities for technical innovations in specific applications such as deep field imaging, and to further develop comprehensive methodologies in these areas. This may also involve comparative studies with other existing probabilistic approaches of noise/source characterization. In addition to filtering-based denoising, there are still other methods that may be used to solve this problem, such as eigenvalue decomposition (Briggs 1995; Rau 2010; Guo et al. 2016). Experiments show that the proposed model estimator is very effective for the reconstruction of a noisy compact emission. The code will be made publicly available.[9] In this work, we focus on the case of narrow-band observations with noisy compact emission, but the wide-band wide-field imaging or a situation with diffuse emission will bring new problems, which is also part of our future work plan.

Software: CASA (McMullin et al. 2007), numpy (Harris et al. 2020), matplotlib (Hunter 2007), Python https://www.python.org.

ORCID iDs

L. Zhang https://orcid.org/0000-0003-1126-3300
M. Zhang https://orcid.org/0000-0002-8315-2848

References

Bhatnagar, S., & Cornwell, T. J. 2004, A&A, 426, 747
Bhatnagar, S., Cornwell, T. J., & Uson, J. M. 2008, A&A, 487, 419

---

[9] https://github.com/lizhangscience/Dn-Clean

Bonaldi, A, 2018, in IAU Symp. 333, Peering towards Cosmic Dawn (Cambridge: Cambridge Univ. Press), 269

Briggs, D. S. 1995, PhD thesis, The New Mexico Institute of Mining and Technology

Clark, B. G. 1980, A&A, 89, 377

Condon, J. J., Cotton, W. D., Greisen, E. W., & Yin, Q. F. 1998, AJ, 115, 1693

Cornwell, T. J. 2008, ISTSP, 2, 793

Cornwell, T. J., & Wieringa, M. 1997, in ASP Conf. Ser. 125, Astronomical Data Analysis Software and Systems VI (San Francisco, CA: ASP), 10

Event Horizon Telescope Collaboration, Akiyama, K., Alberdi, A., et al. 2019, ApJL, 875, L4

Gonzalez, R. C., & Woods, R. E. 2010, Digital Image Processing (3rd edn.; New York: Pearson), 62

Guo, Q., Zhang, C. M., Zhang, Y. F., & Liu, H. 2016, TCSVT, 26, 5

Harris, C. R., Millman, K. J., van der Walt, S. J., et al. 2020, Natur, 585, 357

Högbom, J. A. 1974, A&AS, 15, 417

Hunter, J. D. 2007, CSE, 9, 90

Jia, P., Sun, R. Y., Wang, W. N., Cai, D. M., & Liu, H. G. 2017, MNRAS, 470, 2

McMullin, J. P., Water, B., Schiebel, D., Yound, W., & Golap, K. 2007, in ASP Conf. Ser. 376, Astronomical Data Analysis Software and Systems, XVI, ed. R. A. Shaw, F. Hill, & D. J. Bell (San Francisco, CA: ASP), 127

Portillo Stephen, K. N., Lee Benjamin, C. G., Daylan, T., & Finkbeiner Douglas, P. 2017, AJ, 154, 132

Puetter, R. C., Gosnell, T. R., & Yahil, Amos. 2005, ARA&A, 43, 139

Rau, U. 2010, PhD thesis, New Mexico Institute of Mining and Technology

Rau, U., Bhatnagar, S., & Owen, F. N. 2016, AJ, 152, 124

Rau, U., Bhatnagar, S., Voronkov, M., & Cornwell, T. 2009, Proc. IEEE, 97, 1472

Rau, U., & Cornwell, T. J. 2006, EVLA Memo102

Rau, U., & Cornwell, T. J. 2011, A&A, 532, A71

Schwab, F. R. 1984, AJ, 89, 1067

Sun, R. Y., Yu, S. X., & Jia, P. 2021, AJ, 161, 245

Taylor, G. B., Carilli, C. L., & Perley, R. A. 1999, in ASP Conf. Ser. 180, Synthesis Imaging in Radio Astronomy II (San Francisco, CA: ASP), 127

Thompson, A. R., Moran, J. M., & Swenaon, G. W. 2017, Interferometry and Synthesis in Radio Astronomy (3rd edn.; Berlin: Springer), 767

Vafaei Sadr, A., Vos Etienne, E., Bassett Bruce, A., et al. 2019, MNRAS, 484, 2793

White, R. L., Becker, R. H., Helfand, D. J., & Gregg, M. D. 1997, ApJ, 475, 479

Wilman, R. J., Miller, L., Jarvis, M. J., et al. 2008, MNRAS, 388, 1335

Zhang, L., Bhatnagar, S., Rau, U., & Zhang, M. 2016, A&A, 592, A128

Zhang, L., Mi, L. G., Xu, L., et al. 2021, RAA, 21, 063

Zhang, L., Mi, L. G., Zhang, M., et al. 2021b, A&A, 646, A44

Zhang, L., Mi, L. G., Zhang, M., Liu, X., & He, C. L. 2020, A&A, 640, A80

Zhang, L., Xu, L., & Zhang, M. 2020, PASP, 132, 041001

Zhang, L., Zhang, M., & Liu, X. 2016, Ap&SS, 361, 153